Journal of MATERIALS RESEARCH

Invited Feature Paper
DOI:10.1557/s43578-025-01631-6

EARLY CAREER SCHOLARS IN MATERIALS SCIENCE, 2026

ANNUAL ISSUE

Investigating the impact of nanostructured Nb_2O_5-based coating on the corrosion and corrosion-fatigue resistance of 2198-T8 aluminium alloy

Uriel Darhê Oudinot Dias Rangel[1], Murilo Oliveira Alves Ferreira[1], Natália Bueno Leite Slade[2], Rogério Valentim Gelamo[2], Carlos Antônio Reis Pereira Baptista[3], Haroldo Cavalcanti Pinto[1], Igor Mota[4], Guilherme Yuuki Koga[4], Hugo Manuel Brito Águas[5], Witor Wolf[1], Jéferson Aparecido Moreto[1,a)]

[1] *Materials Engineering Department, São Carlos School of Engineering, University of São Paulo (USP), São Carlos, São Paulo, Brazil*
[2] *Federal University of Triângulo Mineiro (UFTM), Uberaba, Minas Gerais, Brazil*
[3] *Lorena School of Engineering, University of São Paulo (USP), Lorena, São Paulo, Brazil*
[4] *Department of Materials Engineering, Federal University of São Carlos, São Carlos, São Paulo, Brazil*
[5] *Departamento de Ciência Dos Materiais, DCM, Centro de Investigação de Materiais (Lab. Associado I3N)UNINOVA-Instituto de Desenvolvimento de Novas Tecnologias, Lisbon, Portugal*
[a)] Address all correspondence to this author. e-mail: jamoreto@usp.br

Received: 9 May 2025; accepted: 12 June 2025

This investigation examined the efficacy of Nb_2O_5-based coatings, deposited by using the reactive sputtering technique, on the corrosion and corrosion-fatigue behaviour of 2198-T8 aluminium alloy used as aircraft material. Global corrosion behaviour was accessed by Open Circuit Potential (OCP), Potentiodynamic Polarization curves (PPc) and Electrochemical Impedance Spectroscopy (EIS) techniques in 0.6 mol L^{-1} NaCl solution. Fatigue crack growth (FCG) tests were conducted under controlled loading conditions in both air and saline environments. Comprehensive structural and morphological characterisations were performed using advanced microscopy and spectroscopy techniques, including Atomic Force Microscopy (AFM), Scanning Electron Microscopy/Energy Dispersive X-ray Spectroscopy (SEM/EDX), Raman spectroscopy, Fourier Transform Infrared Spectroscopy (FTIR), and Electron Backscatter Diffraction (EBSD). The results unequivocally demonstrated the protective nature of the coating, significantly enhancing the alloy's durability as evidenced by corrosion and fatigue-corrosion tests. These findings underscore the substantial potential of Nb_2O_5 coatings in extending the service life of 2198-T8 aluminium alloy when subjected to aggressive environments, thereby providing invaluable data for aerospace engineering applications.

Jéferson Aparecido Moreto

Jéferson Aparecido Moreto is an Associate Professor in the Department of Materials Engineering (SMM) at the São Carlos School of Engineering (EESC), University of São Paulo (USP), São Carlos, São Paulo, Brazil. Professor Moreto holds a Bachelor of Science degree in Physics from Universidade Estadual do Centro-Oeste (Unicentro), a Master's degree in Materials Engineering from Universidade Federal do Paraná (UFPR), and a PhD in Materials Science and Engineering from USP. He completed a research period at the Mechanical and Materials Technologies Centre (CT2M) at the Universidade do Minho, Portugal. Throughout his career, he has held positions as a visiting professor at Seneca College of Applied Arts and Technology in Canada and at Instituto Superior Técnico (IST) in Lisbon. His main research topics include materials engineering and metallurgy, mechanical properties of metals and alloys, fracture toughness, corrosion, and corrosion-fatigue processes. Additionally, he possesses expertise in condensed matter physics, with an emphasis on structural refinement (Rietveld method), X-ray diffraction, and chemical nanotechnology. Dr. Moreto leads the Electrochemistry, Surface and Corrosion Center (NEESC) and the Mechanical Testing and Failure Analysis Center (NEMAF) at SMM-EESC-USP .

Introduction

Aluminium alloys have established and maintained their status as a crucial material in the aerospace and automotive industry due to their outstanding properties, which include good resistance to global and localised corrosion processes, attributed to the spontaneous formation of Al_2O_3 thin films on the metallic surface when exposed to the environment, an exceptional strength-to-density ratio in comparison to other metals such as steel, as well as lower production costs [1, 2]. Various alloying elements are incorporated into the metallic matrix, seeking to control specific physicochemical properties of aluminium alloys. As is known, Copper (Cu: 2–10 wt%) increases strength and hardness, though it diminishes elongation, Magnesium (Mg: ~ 0.5 wt%) enhances ductility in aluminium-copper alloys, while Lithium (Li: 1–3 wt%) primarily increases the elastic modulus and reduces the density [3]. Elements additions lead to the formation of nanometric and submicrometric particles, often referred to as intermetallic particles (IMs), which can precipitate within the bulk material. These particles may exhibit different electrochemical potentials compared to the matrix, promoting galvanic coupling [4]. Furthermore, the synergistic effects of corrosion and other detrimental processes, such as fatigue, can further adversely affect the operational lifespan of the material in industrial applications.

As previously reported in the literature [4–8], nanometric particles with chemical composition Al_2CuLi, commonly referred to as the T1 phase, are primarily responsible for the strengthening of Al-Cu-Li alloys but are also related to the detrimental effects on the material by exposure to aggressive environments, promoting a severe localised corrosion (SLC) process. Initially, T1 phases preferentially precipitate along dislocation lines and, upon exposure to aggressive environments, act anodically relative to the surrounding aluminium matrix [8]. In the early corrosion stages, aluminium and lithium selectively dissolve from the T1 particles. As corrosion progresses, these particles become copper-enriched, shifting their electrochemical potential to a more noble state. Consequently, galvanic coupling between the nobler T1 phase and the aluminium matrix intensifies, promoting preferential dissolution of the surrounding matrix [9]. Over extended periods, this phenomenon can evolve into a SLC process [6]. Furthermore, as elucidated in reference [4], iron-rich submicrometric particles behave cathodically relative to the matrix, establishing additional galvanic coupling. This cathodic activity accelerates the preferential dissolution of the surrounding bulk material, emphasising the intricate interplay between microstructural characteristics and the electrochemical response of 2xxx series aluminium alloys [10–12].

Aeronautical applications demand a specific combination of properties, including high ultimate tensile strength, superior fatigue and corrosion-fatigue performance, and overall corrosion resistance [1]. However, aluminium and its alloys remain vulnerable to both global and localised corrosion when exposed to aggressive environments, such as sodium chloride solutions, primarily due to their limited repassivation capabilities. Pitting corrosion, one of the most critical degradation mechanisms affecting these materials, arises from the breakdown of the naturally formed oxide films on their surfaces. This breakdown establishes electrochemically active sites that promote the preferential dissolution of the metallic substrate – as previously described – highlighting the crucial role of surface film integrity in preserving mechanical performance [11, 13–15]. Furthermore, to mitigate such effects, additional corrosion resistance can be imparted by applying protective coatings of various types through various deposition techniques [16–19].

Our research group has been focused on developing Nb_2O_5-based coatings, deposited by the reactive sputtering technique, on various materials such as stainless steels, aluminium, and titanium alloys, aiming to enhance their mechanical, corrosion, and biological properties [17, 20–22]. The Nb_2O_5-based coatings deposited on the surfaces of Ti-6Al-4 V, 2524-T3, 2198-T851, 7050-T7451 aluminium alloys, and 316L SS effectively protect these materials from localised corrosion processes. It is widely recognised that pits in the metal matrix serve as stress concentrators, significantly increasing the fatigue crack growth rates (FCGs), resulting in the early onset of short cracks that reduce the number of cycles until material failure. Nevertheless, Nb_2O_5-based coatings offer the promise of enhancing both corrosion resistance and mechanical properties, thereby alleviating these detrimental effects [23–25]. However, the effects of Nb_2O_5 coatings on the corrosion and corrosion-fatigue behaviour of the 2198-T8 aluminium alloy remain unexplored.

In this paper, we introduce an innovative methodology to evaluate the impact of Nb_2O_5 coatings, deposited via the reactive sputtering technique, on the corrosion and corrosion-fatigue behaviour of the 2198-T8 aluminium alloy, a material commonly used in aircraft construction. This investigation is divided into two distinct sections. The first section provides a comprehensive analysis of the effect that Nb_2O_5 coatings have on the global and localised corrosion processes of the 2198-T8 aluminium alloy. The second section examines the influence of Nb_2O_5 coatings on the FCG behaviour of the 2198-T8 aluminium alloy when exposed to a 0.6 mol L^{-1} NaCl solution. To the best of our knowledge, this pioneering study is the first to delve into the advantageous effects of Nb_2O_5 coatings on enhancing the anticorrosive and fatigue-corrosion properties of the 2198-T8 aluminium alloy. Through a meticulous exploration of Nb_2O_5 coatings, we promoted insights that addressed the immediate challenges faced in material degradation and paved the way for future innovations in protective coating technologies.

Results & discussion

Morphology and structure

Figure 1(a) displays a three-dimensional (3D) schematic representation of the 2198-T8 aluminium alloy microstructure, which was revealed by using Keller's reagent for a duration of 12 s. In the S-T direction, elongated grains are observed, indicating the rolling process of the aluminium alloy analysed in this study. The dark spots visible in all micrographs correspond to the micrometric-sized IM particles and inclusions dispersed on the alloy surface. As previously described, the microstructure of the 2198-T8 aluminium alloy is composed of micrometre and nanometre-sized IM particles that play a crucial role in the global and localised corrosion properties. These IMs are formed during the solidification process and exhibit a heterogeneous distribution within the aluminium matrix. The micrometric-sized IM particles are more pronounced, occupying a substantial volume in relation to the aluminium matrix. In contrast, while the nanometre-sized particles are less numerous, they exhibit a significantly higher surface area-to-volume ratio, thereby increasing their impact on the mechanical properties of the 2198-T8 aluminium alloy. Furthermore, the shape and morphology of these particles may impact not only the mechanical strength but also the global and localised corrosion processes of the 2198-T8 aluminium alloy when exposed to a solution containing aggressive ions. Fig. 1(b) displays a micrograph of the surface of the 2198-T8 aluminium alloy obtained by SEM technique, revealing the presence of dispersed IM particles. As reported by Moreto and colleagues [4], the IM particles indicated by the yellow arrows [see Fig. 1(b)] are enriched in iron

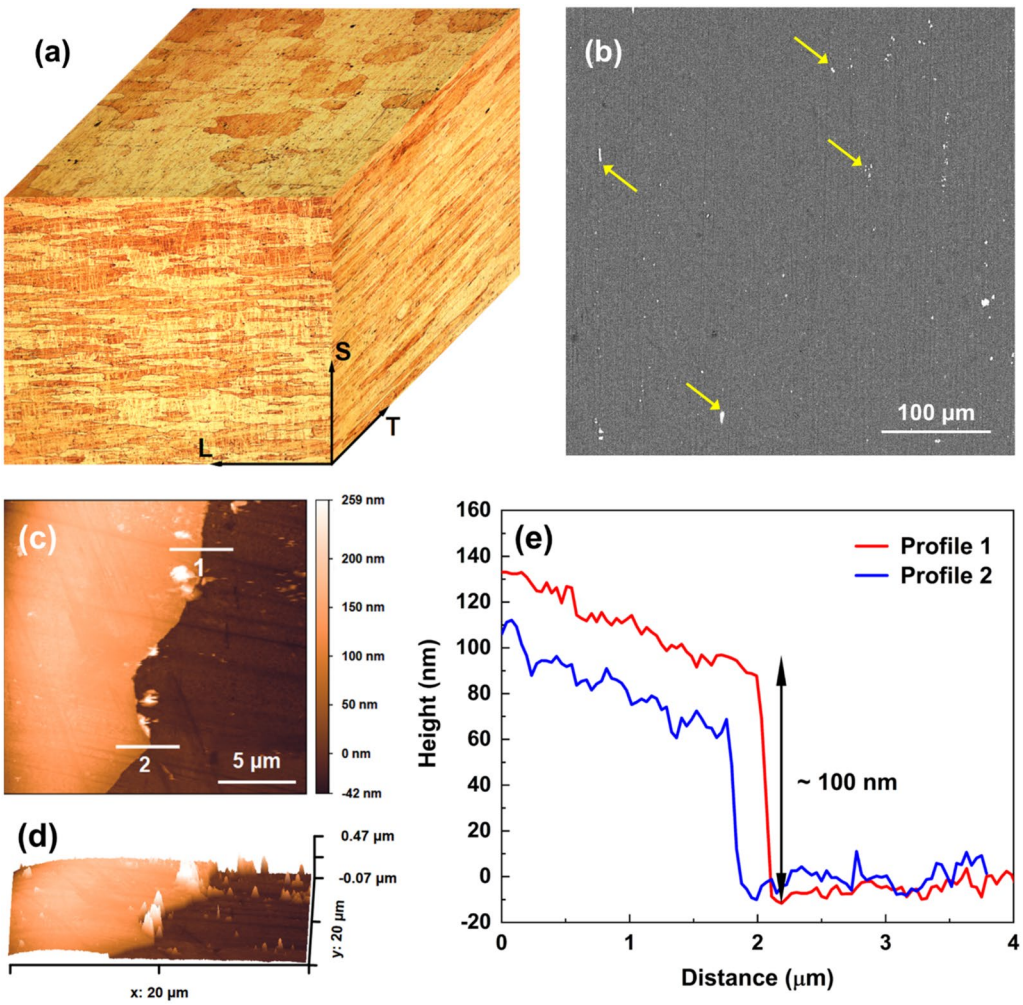

Figure 1: (a) Schematic representation of the 3D microstructure of the 2198-T8 aluminium alloy obtained via optical microscopy following a 15 s attack with Keller's reagent; (b) SEM micrograph of the surface of the 2198-T8 aluminium alloy, illustrating the presence of dispersed micrometre-sized IM particles within the aluminium matrix. The presented micrograph was obtained in the BSE mode; (d) 2D morphology projection of the 2198-T8 aluminium alloy containing Nb_2O_5 thin films; (c) 3D morphology projection; (e) graphical representation illustrating the thickness profiles of the Nb_2O_5 coatings.

(Fe) and copper (Cu), functioning as cathodes in relation to the aluminium matrix. The identification of the highlighted particles as Al_7Cu_2Fe was corroborated by EDX; however, the associated spectra are not included in this study.

The beneficial properties of the Nb_2O_5-based coating have been demonstrated in several studies conducted by our research group. The coatings produced have been extensively characterised both morphologically and structurally and more information can be found in the following references [17, 18, 20–25]. Nevertheless, we have opted to present select morphological and structural characterisation results that will facilitate a more comprehensive discussion of the corrosion and corrosion-fatigue findings. The Nb_2O_5 coating deposited on the surface of the 2198-T8 aluminium alloy was evaluated using AFM technique, as shown in Fig. 1(c–e). The 2D and 3D projection presented in Fig. 1(c, d) highlights two distinct regions of the 2198-T8 aluminium alloy, coated and uncoated areas. By analysing the height profile, a thickness of approximately 100 nm was determined. These corresponding values are depicted in Fig. 1(e). The AFM analysis demonstrates the effective adhesion of the Nb_2O_5 coating, which may provide a continuous barrier against aggressive media, thereby enhancing the alloy's durability and resistance to corrosion and corrosion-fatigue, as will be discussed in the subsequent sections of the manuscript.

Considering the FTIR spectrum presented in Fig. 2(a), two distinct regions are displayed: an inset illustrating the complete spectral range analysed and a section of particular interest, detailed between 2000 and 400 cm^{-1}. The spectral range from 1000 to 400 cm^{-1} features a broad band resulting from the overlap of contributions from bands centred at approximately

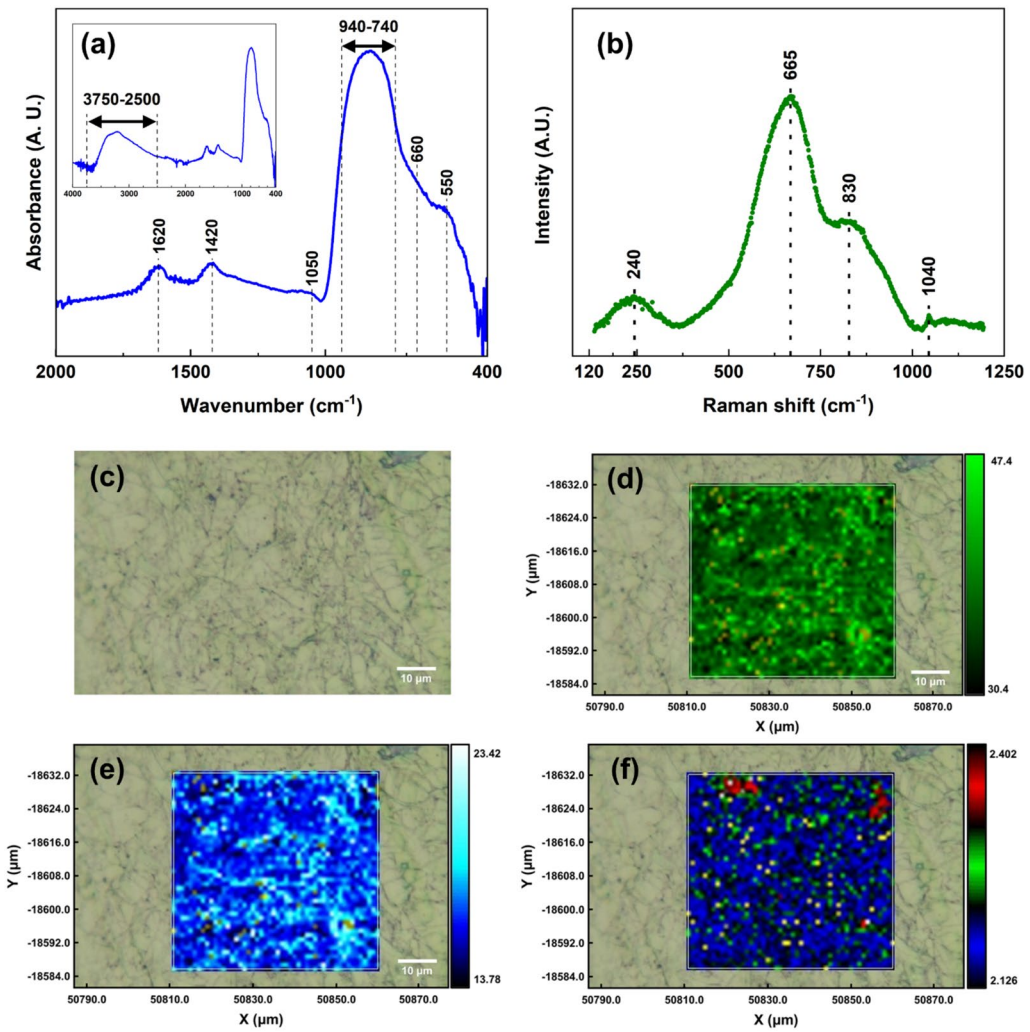

Figure 2: (a) FTIR-IRRAS spectrum obtained at 70° p-polarized for Nb_2O_5 nanostructured film. The dashed lines are a guide for the eyes; (b) Representative Raman spectrum for Nb_2O_5 thin film deposited over multilayer graphene paper by reactive sputtering; (c) Optical image of Nb_2O_5 thin film surface using the micro-Raman system and illustrating the mapped film region; (d) maps of 665 cm^{-1}; (e) maps of 830 cm^{-1}; (f) map of the ratios between intensities of 665 cm^{-1}/830 cm^{-1}.

940 and 840 cm^{-1}, which are attributed to the Nb = O stretching in Nb_2O_5 as well as Nb–O stretching. Additionally, bands centred at approximately 605 and 510 cm^{-1} correspond to the Nb–O-Nb stretching modes in-plane and out-of-plane, respectively [26, 27]. A low-intensity shoulder observed between 1150 and 1000 cm^{-1} is associated with the Nb = O stretching of Nb_2O_5 and its isomer [24]. The bands at 1621 and 1422 cm^{-1} are linked to the presence of water adsorbed on the film surface (hydroxyl groups), and carbon dioxide (CO_2), respectively. The pronounced and intense band observed between 3750 and 2500 cm^{-1} is attributed to the OH stretching vibrations of H_2O molecules that are also absorbed on the surface of the film.

A representative spectrum of the 100 nm thick- Nb_2O_5 sample is exhibited in Fig. 2(b), resulting in 3 bands centered at 240, 665, and 830 cm^{-1}, respectively. In addition, a low intensity peak at 1040 cm^{-1} may be also verified. Niobium pentoxide synthesised at temperatures below 300 °C exhibits a significant presence of an amorphous phase interspersed with regions of crystallinity [24, 26, 27]. This structural configuration results in broad spectral bands. The amorphous structure comprises distorted NbO_6 octahedra, NbO_7 pentahedra, and NbO_8 hexahedra as its fundamental structural units [24]. Due to the presence of these various polyhedral, a strong and broad Raman band centred around ~ 650 cm^{-1} is attributed to the symmetric stretching mode of the niobium polyhedral, which shifts to a higher frequency as the degree of crystallinity increases [26]. Additionally, the band centred at ~ 240 cm^{-1} is assigned to the Nb–O-Nb deformational mode [24]. For synthesised niobium pentoxide at temperatures between 300 and 500 °C, the most stable phase is the TT-phase [24, 27]. Its Raman spectrum features bands corresponding to the Nb–O terminal stretch at 911 cm^{-1}, as well as the Nb–O stretch arising from the totally symmetric mode of niobium oxide polyhedral at 660 cm^{-1} [28]. Additionally, the infrared and Raman spectra of inorganic and coordination compounds [29] reveal a Nb–O-Nb deformational mode at 215 cm^{-1}. Furthermore, Nb_2O_5 displays a band at approximately 830 cm^{-1}, which is attributed to the NbO_4. The weak band around 1040 cm^{-1} is characteristic of the symmetric stretching modes of the Nb = O terminal bond [27]. This band may be associated with edge-sharing octahedra, which are notably distorted due to variations in niobium-oxygen bonding [26]. Considering the spectrum presented in Fig. 2(b), it can be inferred that the Nb_2O_5 thin film examined in this study comprises both amorphous and crystalline phases. Through Raman mapping, we investigated the uniformity of the film from a chemical structural perspective. Figure 2(c) displays the image acquired using the optical microscope integrated with the Raman spectrometer, utilising a 100 × objective lens. This specific area of the image underwent Raman mapping, with the resulting maps of the bands centered at 665 and 830 cm^{-1}, as well as the intensity ratio of the 665/830 bands, illustrated in Figs. 2(d–f). The intensities of both bands demonstrate good uniformity, indicating the consistency of the chemical structure of the film deposited via reactive sputtering. Figure 2(f) presents a map of the intensity ratio of the 665/830 bands, revealing that the ratio remains uniform at approximately 2.15 across most of the area, except for two small regions in the upper part of the map. Notably, these regions exhibit some irregularities [as shown in Fig. 2(b)], likely attributed to the multilayer graphene substrate used in the study. This variation in the intensity ratio is probably due to defects associated with the substrate.

Corrosion behaviour

As emphasised in the literature and summarised in this study, aluminium alloys exhibit substantial corrosion resistance, primarily due to the natural formation of a passive oxide layer on their surface when exposed to oxygen [13–15]. However, when aluminium and its alloys are exposed to an aggressive environment, such as chloride containing solutions, this oxide layer proves insufficient to protect against both uniform and localised corrosion processes [30]. In this sense, the Nb_2O_5 protective coatings emerge as promising alternatives for enhancing resistance to both global and localised corrosion of the 2198-T8 aluminium alloy used as aircraft material.

Figure 3(a) displays the OCP curves, obtained over a duration of 7200 s, for the 2198-T8 aluminium alloy, both with and without the Nb_2O_5 coating, exposed to 0.6 mol L^{-1} NaCl solution. The assessment of potential behaviour over immersion time is of paramount importance, as stable potential values indicate good resistance to corrosion process, while fluctuations may suggest ongoing corrosive reactions. Results indicate that the uncoated material exposed to 0.6 mol L^{-1} NaCl solution displays an E_{ocp} value of approximately -0.72 V/SCE. The 2198-T8 aluminium alloy containing the Nb_2O_5 coating demonstrates initial stability only after 3700 s, suggesting significant competition between the anodic and cathodic zones on the surface. The stability of the 2198-T8/Nb_2O_5 sample was maintained until the conclusion of the experiment, which lasted for 7200 s, 40 mV/SCE towards less negative values compared to the bare material.

The characteristic PPc obtained for the 2198-T8 and 2198-T8/Nb_2O_5 specimens are presented in Fig. 3 (b, c), respectively. Figures 3(d–g) present a schematic representation of images acquired through optical microscopy of the 2198-T8 alloy, both with and without coatings, following the PP tests, showing regions of pit agglomerates [Fig. 3(d)], SLC process appearance (Fig. 3(e) as well as regions of delamination in the coated material [Figs. 3(f, g)]. A general analysis of the PPc reveals that the E_{corr} of the 2198-T8/Nb_2O_5 alloy is shifted to a less negative value compared to the base material, indicating improved thermodynamic stability against corrosion processes. As reported in reference [20], the E_{corr} value is typically

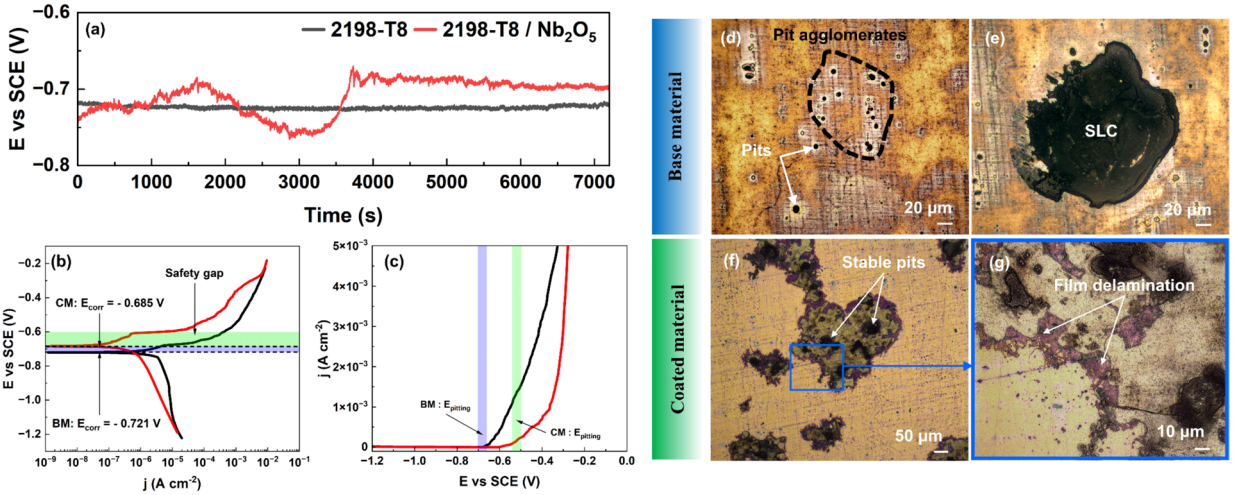

Figure 3: Electrochemical response of 2198-T8 aluminium alloy and its Nb_2O_5-coated counterpart on a 0.6 mol L^{-1} NaCl solution, and the associated corrosion morphologies. (a) OCP variation with time for 2198-T8 and 2198-T8/Nb_2O_5; (b) PPc obtained for both 2198-T8 and 2198-T8/Nb_2O_5 systems; (c) *j* (A cm^{-2}) *versus* E/SCE (V) representation for the $E_{pitting}$ determination; (d) regions of pit agglomerates; (e) SLC process appearance; (f) regions of delamination in the coated material.

viewed as an indication of the nobility of the material, with a less negative E_{corr} corresponding to a more corrosion-resistant system. As demonstrated in the analysis of the 2198-T8 aluminium alloy, where the absence of a passive plateau in the anodic domain is observed, it is noted that the growth of pits intensifies with an increase in electrical current. Thus, one can infer that pitting corrosion manifests naturally at E_{corr}. EIS, Kelvin Probe technique (SKP), and scanning vibrating electrode technique (SVET) have been employed in [4] to investigate the behaviour relating to global and localised corrosion of 2524-T3, 2198-T851, 7050-T7451, and 7081-T7351 aluminium alloys when exposed to 0.6 mol L^{-1} NaCl solution, finding that E_{corr} and the pitting potential ($E_{pitting}$) possess very similar values.

Figure 3(c) represented as *j* (A cm^{-2}) *versus* E/SCE (V), illustrates that E_{corr} and the $E_{pitting}$ are quite close for the 2198-T8 aluminium alloy, indicating that a slight fluctuation in potential values leads to an increase in current density. Considering the 2198-T8/Nb_2O_5 alloy, it is noted that there exists a difference of 97 mV/SCE between E_{corr} and $E_{pitting}$, which can be viewed as a safety margin. In other words, $E_{pitting}$ cannot be determined at E_{corr}. Finally, when comparing the uncoated and coated 2198-T8 aluminium alloys, the former exhibits an i_{corr} value that is an order of magnitude higher, 0.37 µA *versus* 0.017 µA.

The EIS results for the 2198-T8 aluminium alloy, both with and without Nb_2O_5 thin films, at various immersion times (3, 6, 12, 24, 72, and 168 h) when exposed to a 0.6 mol L^{-1} NaCl solution are illustrated by the Bode and Nyquist diagrams, as presented in Fig. 4, respectively. These diagrams were obtained sequentially for the same sample and thus represent the evolution of the electrode response as a function of the immersion time in the 0.6 mol L^{-1} NaCl solution. All tests were conducted in triplicate and exhibited good reproducibility. Furthermore, to ensure the consistency of the impedance data and its compliance with validation criteria, Kramers–Kronig (KK) transforms were employed.

A general analysis of the EIS results indicates the presence of an oxide film on the metallic matrix, which is responsible for a time constant at high frequencies. Additionally, a second time constant is evident at low frequencies, possibly due to pitting corrosion. The results further indicate that, even with prolonged exposure time, the coated material demonstrates a higher impedance modulus (|Z|), highlighting the positive influence of the Nb_2O_5 thin film on enhancing the corrosion properties of the 2198-T8 aluminium alloy. Moreover, in the transition region from high to intermediate frequencies, the |Z| for the coated sample displayed higher values compared to the base material, which persists in the low-frequency range. Regarding the phase angle (-ϕ), although the peak shifts to a lower value for the coated material compared to the uncoated one, the peak region extends over the intermediate frequency range, suggesting a prolonged retention of the capacitive characteristics of the 2198-T8/Nb_2O_5 electrode when exposed to a solution containing chloride ions. In the supplementary material (SM), as illustrated on Figure SM1, by the Bode spectrum [Figure SM1(a)] and Nyquist diagrams [Figure SM1(b) and SM1(c)], the 2198-T8 aluminium alloy coated with a Nb_2O_5 thin film, when exposed to 0.6 mol L^{-1} NaCl solution for 168 h, demonstrated significantly superior performance compared to the uncoated material immersed in the same solution for just 3 h. These findings consistently corroborate the protective capability of the Nb_2O_5 coating, which

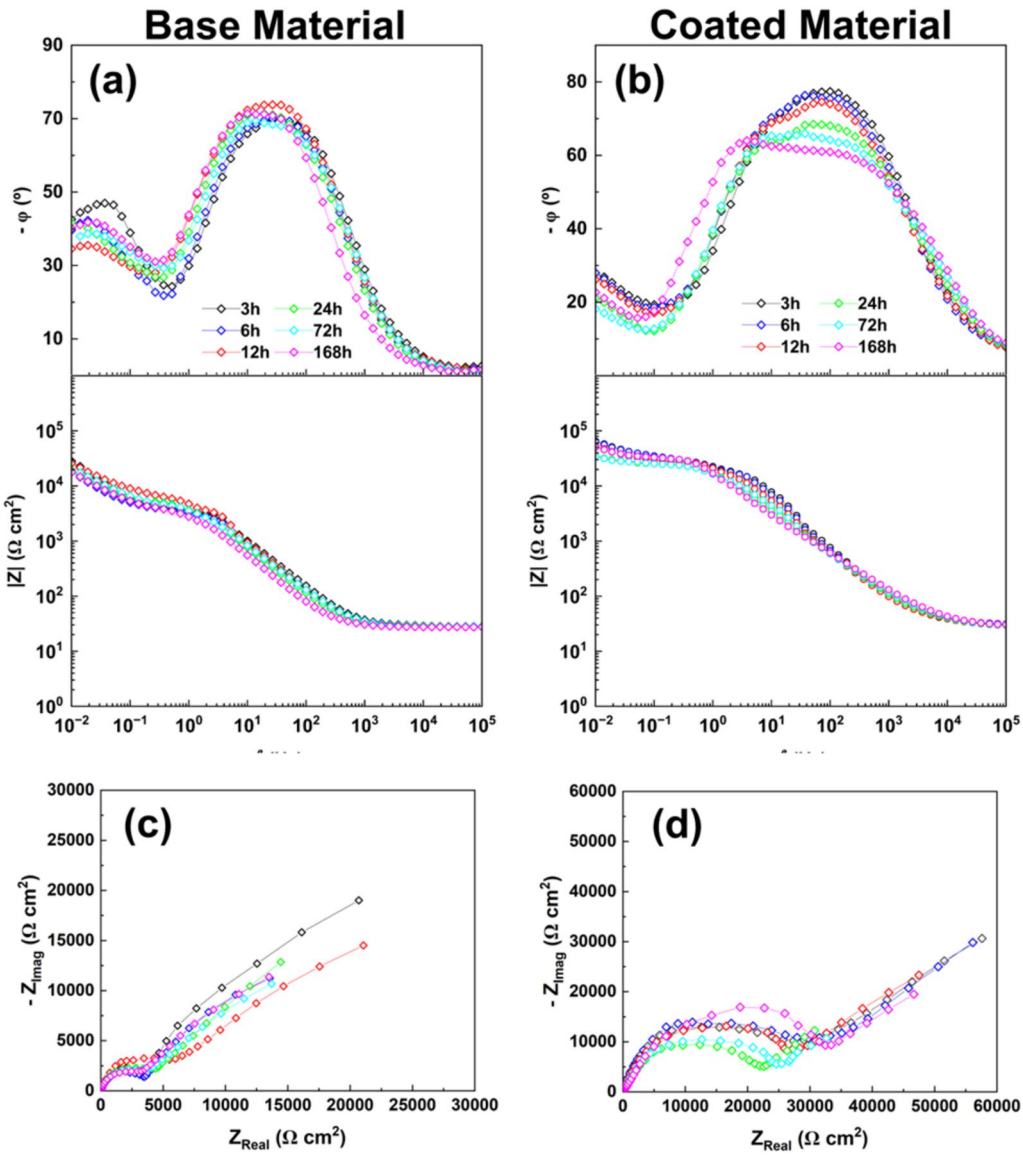

Figure 4: Bode plots of EIS spectra of (a) uncoated; (b) coated 2198-T8 aluminium alloy exposed to 0.6 mol L^{-1} NaCl solution; Nyquist diagrams of EIS spectra of (c) uncoated and (d) coated 2198-T8 aluminium alloy exposed to 0.6 mol L^{-1} NaCl solution.

was deposited on the surface of the 2198-T8 alloy using the reactive sputtering technique.

In a present work, an equivalent electrical circuit (EEC) was proposed to understand the corrosion mechanisms associated to the 2198-T8 and 2198-T8/Nb_2O_5 samples when exposed to 0.6 mol L^{-1} NaCl solution. The EEC displayed in Fig. 5(a) is composed by R_Ω, ohmic resistance of the electrolyte, a loop R_{ox}-CPE_{ox}, respectively the resistance and phase element constant of the oxide layer, and a contribution of the pitting/trenching processes taking place at the particles as a R_{ct}-CPE_{dl} network that represents the charge transfer reaction corresponding to localised corrosion and the capacitance of the double layer, added to the additional resistance of the electrolyte inside the pit/trench, R'_Ω. It is very important to emphasize that the measured values R_{ox}, CPE_{ox}, R'_Ω, R_{ct}, and CPE_{dl} depend on the pitted area fraction θ. In this sense, the mentioned parameters may be written as $R^*_{ox}/(1-\theta)$, $(1-\theta)CPE^*_{ox}$, $R^{*'}_\Omega/\theta$, R^*_{ct}/θ and θCPE^*_{dl}, where R^*_{ox}, CPE^*_{ox}, $R^{*'}_\Omega$, R^*_{ct} and CPE^*_{dl} are the intrinsic values of each parameter. As is known, $R_{ox}/(1-\theta)$ tends to be extremely high, not allowing for any conduction of electrons across the oxide film. So, this circuit element was removed from the EEC presented in Fig. 5(a), generating the EEC used for fitting the experimental data [see Fig. 5(b)]. The Bode plots [Figs. 5(c, d)] and the Nyquist diagrams [Fig. 5(e)] illustrate the data fitting for the 2198-T8 and 2198-T8/Nb_2O_5 specimens in the first moment of tests, specifically after 3 h of immersion. As can be seen, the

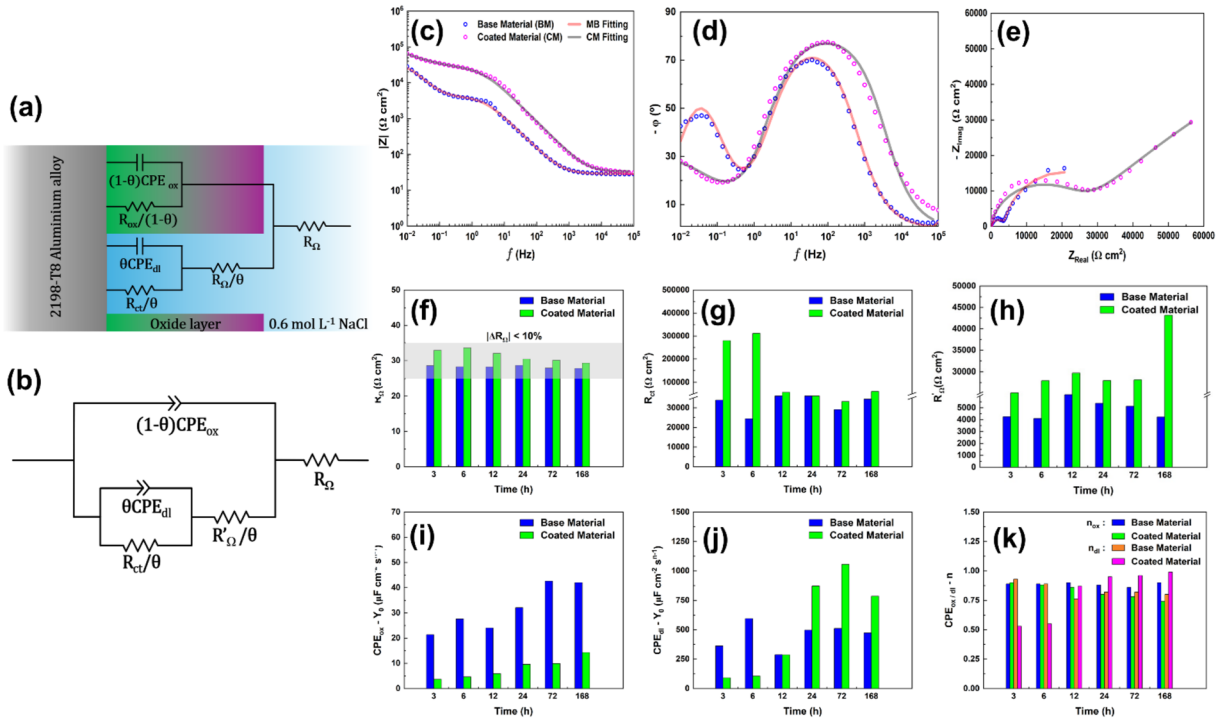

Figure 5: (a) Schematic representation of the corrosion and the proposed EEC; (b) EEC used for fitting the experimental data; (c–e) Bode plots and Nyquist diagrams of EIS spectra and fitting of coated and uncoated 2198-T8 alloy; (f–k) Average values of the EIS parameters.

impedance spectra were fitted to this circuit, resulting in a very good correlation, with χ^2 values in the range of 10^{-4}—10^{-3}. Here, the phase constant elements will be treated as capacitance. So, the phase constant elements (CPE_{ox} and CPE_{dl}) will be treated as capacitance (represented as C_{ox} and C_{dl}). The authors contend that, more significant than determining the actual capacitance values, is gaining an understanding of the corrosion mechanisms associated with the varying immersion times. Figures 5(f-k) provide the typical values of the fitting results parameters for 2198-T8 and 2198-T8/Nb_2O_5 samples. As previously reported in reference [4], these findings were anticipated, given that the distance between the working and reference electrodes (WE and RE) was kept constant throughout the EIS tests. Furthermore, considering that the maximum immersion time examined was 168 h, no significant evaporation of the solution occurred [see Fig. 5(f)]. As previously explained, the parameter R'_Ω describes the solution resistance within the pit. The general trend of decreasing R'_Ω for the 2198-T8 aluminium alloy when compared to the coated material can be attributed to an increase in the pitted surface area [Fig. 5(g)]. Regarding the values obtained for the charge transfer resistance, R_{ct}, and considering that $R_{ct} = R_{ct}^{*} (A_{geom}/A_{pit})$, it can be inferred that higher R_{ct} values are directly associated with a smaller pit area [see Fig. 5(h)], thereby demonstrating the potential effectiveness of the Nb_2O_5 coating produced by reactive sputtering technique produced in the present work. The values of CPE_{ox}, across all immersion times, consistently remain higher for the base material. Considering the oxide capacitance, C_{ox}, may be written as $C_{ox} = (k \varepsilon_0 S)/d$, where ε_0 is the permittivity of the vacuum (8.85×10^{-12} F/m), k is the dielectric constant of the oxide film, S the sample surface area and d the thickness, the highest C_{ox} values for the 2198-T8 aluminium alloy are directly associated with its lower resistance to the corrosion process when compared to 2198-T8/Nb_2O_5 thin film in aggressive medium containing Cl^- ions. Considering the 2198-T8 aluminium alloy, the C_{dl} values tend to increase significantly during the first 12 h of immersion in 0.6 mol L^{-1} NaCl solution. These finds may be attributed to the growth of pits, an increase in the pitted surface area, or, to the heightened acidification of the internal pit environment. After 24 h of immersion an opposite effect is observed, allowing us to assume the action of corrosion products in sealing electroactive regions in the base material. The n_{ox} and n_{dl} values are between 0.86–0.90 and 0.76–0.93 for the 2198-T8 aluminium alloy. Considering the coated specimen, the n_{ox} and n_{dl} values are 0.74–0.90 and 0.53 – 0.98, respectively. Here, n is an empirical characteristic parameter derived from the fitting process, which is linked directly to the non-uniformity of the current distribution on the material surface. The relationship between the parameter n and the impedance of a constant phase element

is given by, $Z_{CPE} = 1/Y_0(jw)^n$, where Y_0 is the admittance (F cm^{-2} s^{n-1}) and w angular frequency (rad s^{-1}).

Figure 6(a–d) and (e–j) present a schematic representation derived from SEM/EDX analysis of the surfaces of the 2198-T8 and 2198-T8/Nb_2O_5 aluminium alloys following EIS tests. Figure 6(a) offers a comprehensive depiction of the surface of the 2198-T8 aluminium alloy, underscoring the presence of aluminium oxide particles dispersed throughout the metallic matrix. This oxide is substantiated by the EDX mapping illustrated in Fig. 6(b). Furthermore, Figs. 6(c) and (d) exemplify the

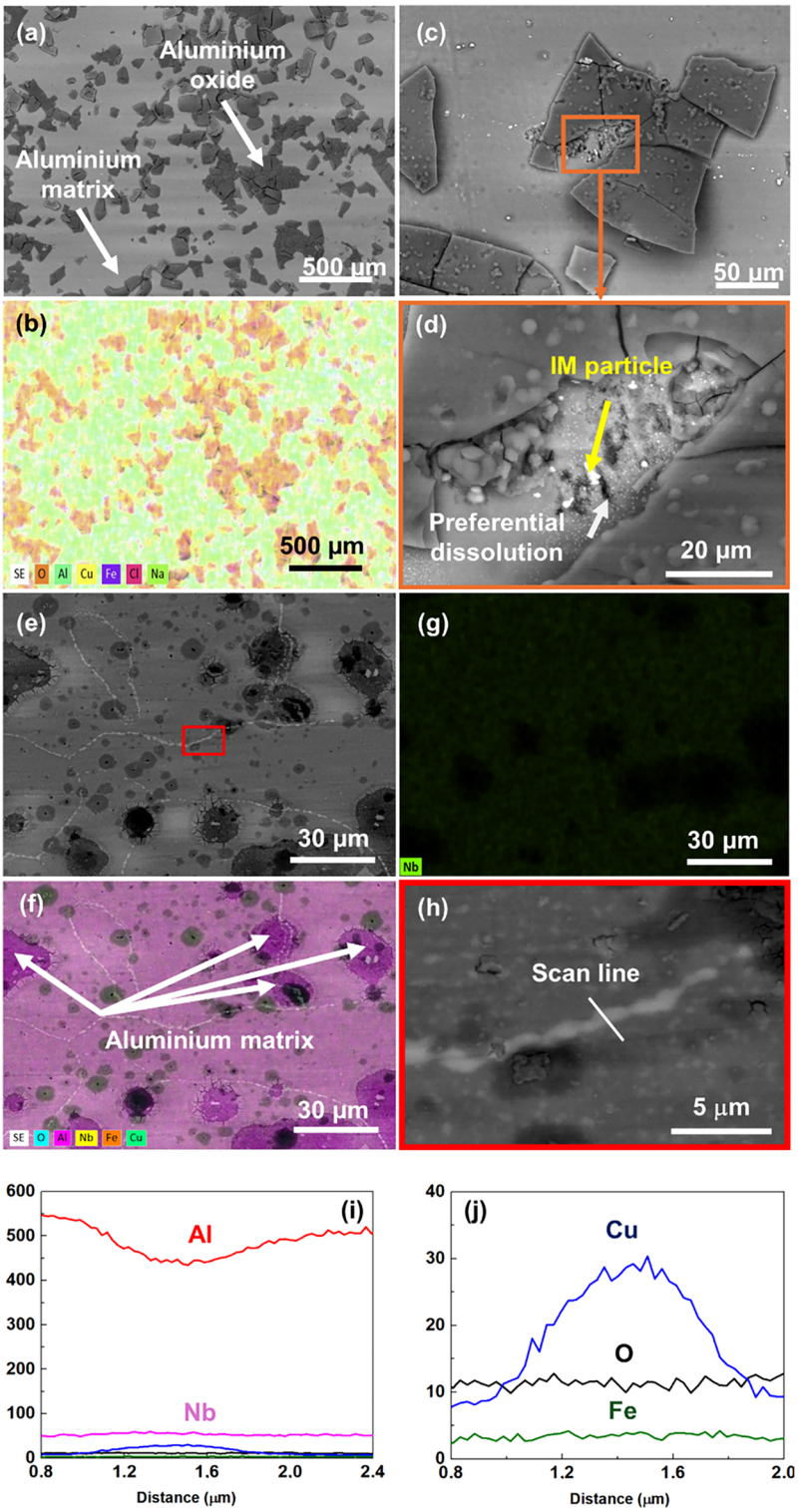

Figure 6: Surface morphology of the (a–d) uncoated and (e–h) coated 2198-T8 aluminium alloy following EIS tests. (a) an overview of the aluminium matrix, illustrating the dispersion of oxides throughout the metallic matrix; (b) EDX map displaying the presence of the elements O, Al, Cu, Fe, Cl, and Na; (c) a detailed view of a specific region, highlighting the galvanic coupling process between a micrometric IM particle and the aluminium matrix; (d) evidence of a preferential dissolution process. (e) an overview of the aluminium matrix, revealing the absence of the coating at specific points; (f) and (g) EDX maps displaying the presence of the O, Al, Cu, Fe, and Nb elements; (h) an enlargement of a specific region from the image presented in Figure 6(e), and (i, j) elemental chemical composition graphs (% in weight) obtained from Figure 6(h), highlighting the presence of Cu on the 2198-T8 aluminium alloy surface.

galvanic coupling process occurring between micrometric IMs and the aluminium matrix, thereby emphasising the relevance of effective coating techniques as mitigation strategies to safeguard the alloy against corrosive attacks. Conversely, Figs. 6(e-j) present the morphology of the 2198-T8 aluminium alloy containing Nb_2O_5 coating after EIS testing. Figure 6(e) highlights phenomena reminiscent of delamination processes on the 2198-T8/Nb_2O_5. These observations are consistent with the EDX maps presented in Figs. 6(f) and (g), respectively. Figure 6(h) offers a magnification of a specific region of the image shown in Fig. 6(e) (indicated by the red box), confirming an increased concentration of copper on the 2198-T8 alloy surface. The corresponding spectra are presented in Figs. 6(i, j) provide further evidence of this alteration in elemental composition. Probably, the copper segregation on the 2198-T8 surface is directly linked to the phenomenon of localised corrosion due to the nanometric intermetallic phase Al_2CuLi.

Corrosion-fatigue performance

The fatigue crack growth (da/dN) as function of stress intensity factor (ΔK), represented as da/dN *versus* ΔK curves, for the 2198-T8 aluminium alloy tested in air, as well as for the 2198-T8 and 2198-T8/Nb_2O_5 samples exposed to 0.6 mol L^{-1} NaCl solution, are presented in Fig. 7(a). As can be seen, a linear correlation between da/dN and ΔK, $9 < \Delta K < 20$ MPa $\sqrt{m}$ was noted. However, the da/dN *versus* ΔK curves deviate from linearity for 1E-5 < FCG < 1E-3 mm/cycle. Overall, it can be observed that the aggressive medium shifted the FCG rates to higher values when compared to the base material for ΔK values up to 14 MPa $m^{1/2}$. Subsequently, the FCGRs of both, the coated and uncoated specimens, tested in a 0.6 mol L^{-1} NaCl solution exhibited a reduction in comparison to those of the 2198-T8 aluminium alloy tested in air, suggesting a modification in the synergistic corrosion-fatigue mechanism. It is well established that various mathematical models can be employed to describe a material's behaviour in the context of corrosion-fatigue, offering valuable insights into the underlying mechanisms. In other words, by incorporating several factors such as the effects of environmental conditions, stress intensity factor as well as material properties, one can predict the propagation of fatigue cracks under corrosive conditions. As cited in [31] and proposed by [32], the rate of fatigue crack growth (FCG) in an aggressive environment, denoted as $(da/dN)_{CF}$, comprises three components: (i) the rate of FCG in an inert environment, $(da/dN)_{in}$, which reflects the contribution of the pure fatigue process, (ii) a cycle-dependent component, $(da/dN)_{cl}$, that demands the synergistic interaction of fatigue and environmental attack, and (iii) $(da/dN)_{cr}$, which arises from the reaction between the environment and the fresh crack surfaces produced by fatigue. In addition, considering highly reactive alloy-environment systems, this contribution also depends on the rate of transport of the aggressive environment to the crack tip. Equation 1 summarizes the three contributions described above to the synergistic fatigue-corrosion process.

$$\left(\frac{da}{dN}\right)_{CF} = \left(\frac{da}{dN}\right)_{inert} + \left(\frac{da}{dN}\right)_{cl} + \left(\frac{da}{dN}\right)_{cr} \quad (1)$$

The corrosion and corrosion-fatigue synergism on the base metal and nugget zone of the 2524-T3 aluminium alloy joined by FSW has been discussed in [31]. As mentioned by the authors [31], for the sake of simplicity and due to the lack of detailed materials information, such as results related to fatigue crack growth in vacuum, the Paris and Erdogan model (see Eq. 2) may be employed for the subsequent discussion. In this regard, the same methodology utilised by the mentioned authors herein will be adopted to simplify the discussions and enhance the understanding of the synergistic corrosion-fatigue processes. For a particular material and a defined set of testing conditions, the behaviour of crack growth can be characterised by the correlation between the cyclic crack growth rate, da/dN, and the stress intensity range, ΔK. At intermediate values of ΔK, there is often a linear trend on the log–log plot, as represented by Eq. 2. Here, $C\left[\frac{(mm/cycle)}{(MPa\sqrt{m})^m}\right]$ and m (dimensionless) are constants of the studied material.

$$\frac{da}{dN} = C\Delta K^m \quad (2)$$

Figure 7(a–c) also exhibit the FCG curves of 2198-T8 and 2198-T8/Nb_2O_5 tested in air and 0.6 mol L^{-1} NaCl solution conditions with their respective linear regressions from the data extracted exclusively from the Paris and Erdogan (region II). Moreover, Fig. 7(d) provides a direct comparison of the obtained linear regressions. The table in Fig. 7 summarises the parameters obtained from the fitted regions using Paris-Erdogan's law. The regression was obtained from 9 to 20 MPa $\sqrt{m}$, allowing the parameters $m = 2.97$ and $C = 1.15 \times 10^{-7}(\text{mm/cycle})/(\text{MPa}\sqrt{m})^m$ for the 2198-T8 sample tested in air, $m = 1.93$ and $C = 1.76 \times 10^{-6}(\text{mm/cycle})/(\text{MPa}\sqrt{m})^m$ for the 2198-T8 sample tested in 0.6 mol L^{-1} NaCl solution, and $m = 2.17$ and $C = 9.32 \times 10^{-7}(\text{mm/cycle})/(\text{MPa}\sqrt{m})^m$ for the 2198-T8/Nb_2O_5 exposed to 0.6 mol L^{-1} NaCl solution. Considering the Paris Edorgan's law parameters displayed in the table, it can be inferred the detrimental impact of the aggressive environment on the FCG curves for the coated and uncoated 2198-T8 aluminium alloy subjected to testing in a 0.6 mol L^{-1} NaCl solution, when compared to the air condition. However, when comparing the materials tested in a 0.6 mol L^{-1} NaCl solution, a positive influence of the Nb_2O_5 thin film can be observed. In

Fitting Conditions	Paris Edorgan's law Parameters C	m	Equation (da/dN =)	Exponential law Parameters A	β	Equation (da/dN =)
Uncoated (Air)	1.15E-7	2.97	1.15E-7 $\Delta K^{2.97}$	7.46E-3	- 44.68	7.46E-3 exp(-44.68/ΔK)
Uncoated (0.6 mol L^{-1})	1.76E-6	1.93	1.76E-6 $\Delta K^{1.93}$	2.21E-3	-27.76	2.21E-3 exp(-27.76/ΔK)
Coated (0.6 mol L^{-1})	9.32E-7	2.17	9.32E-7 $\Delta K^{2.17}$	2.81E-3	-31.55	2.81E-3 exp(-33.55/ΔK)

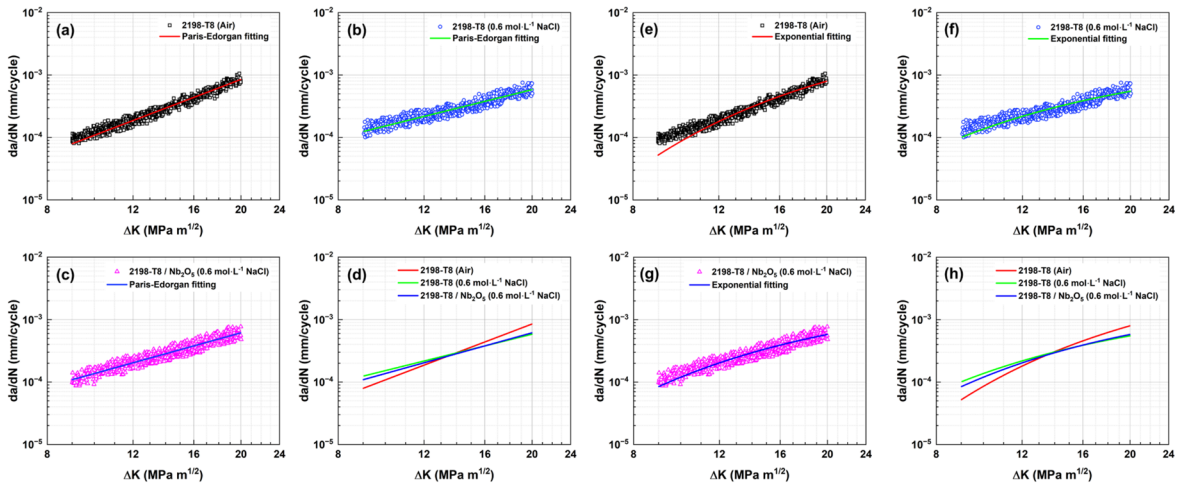

Figure 7: A summary of the parameters derived from the fitted regions employing both Paris-Erdogan's and Exponential laws. (a–c) FCG curves linear regressions from the data extracted exclusively from Paris regime (region II) of 2198-T8 and 2198-T8/Nb_2O_5 in air and 0.6 mol L^{-1} NaCl; and (d) a comparison between the fittings; (e–h) FCG curves exponential fittings from the data extracted exclusively of the region II on the 2198-T8 and 2198-T8/Nb_2O_5 in air and 0.6 mol L^{-1} NaCl complemented by (h) a comparison between the fittings.

other words, for the same DK interval, *C* parameter is lower for the coated sample (9.32×10^{-7} (mm/cycle)/(MPa $\sqrt{m}$)^m *versus* $C = 1.76 \times 10^{-6}$ (mm/cycle)/(MPa $\sqrt{m}$)^m), suggesting the positive impact of the produced coating by the reactive sputtering technique on the 2198-T8 aluminium alloy surfaces.

In the current study, in addition to the fittings derived from the Paris-Erdogan law, we employed the exponential model proposed in [33] to elucidate the influence of the corrosive environment on the FCG curves. This model was specifically designed to capture a certain degree of non-linearity, characterised by slight changes in the slope of Region II da/dN-ΔK plots, observed in metals like titanium and aluminium alloys [33]. And indeed, looking at the results presented, the model appears as a potential tool. For a single FCG curve, this Arrhenius-type relationship, referred to as the *ab* model, may be expressed as Eq. 3. It is important to emphasize that the a and b are fitting coefficients. This model can be readily generalised for a range of stress ratios by expressing *b* in terms of log (R), as illustrated in Eq. 4. Here, β_0 as well as β_1 parameters may be determined by a simple regression. The table of Fig. 7 also presents the parameters obtained from the application of the exponential law, and Fig. 7(e–g) illustrate the experimental FCG curves, along with the corresponding exponential fittings for Region II. These data are specifically for the 2198-T8 and 2198-T8/Nb_2O_5 aluminium alloy, analysed in both air and a 0.6 mol L^{-1} NaCl solution.

$$\frac{da}{dN} = Aexp\left(\frac{\beta}{\Delta K}\right) = e^{\alpha} e^{\left(\frac{\beta}{\Delta K}\right)} \tag{3}$$

$$\beta = \beta_0 + \beta_1 \log(R) \tag{4}$$

A comprehensive analysis indicates that the exponential model employed in this study successfully captures the entirety of Region II for the 2198-T8 aluminium alloy, both with and without the Nb_2O_5 coatings, when tested in a medium containing 0.6 mol L^{-1} NaCl solution [see Figs. 7(b) and (c)]. This finding underscores the model's effectiveness in accurately representing the FCG behaviour of the aluminium alloy when exposed to an aggressive medium. Considering the 2198-T8 aluminium alloy tested in air [Fig. 7(e)], a discrepancy can be verified between the experimental data and the proposed model for $9 < \Delta K < 11$ MPa $\sqrt{m}$. Fig. 7(h) displays a comparative analysis of all the fittings obtained for the 2198-T8 aluminium alloy, both with and without the protective coating, tested in air and in a 0.6 mol L^{-1} NaCl solution. Moreover, a comparison of the latter two conditions reveals the beneficial effect of the Nb_2O_5 coating in reducing the FCGRs, highlighting its potential for enhancing the material's resistance to fatigue under corrosive environment. However, when considering $\Delta K = 14$ MPa $\sqrt{m}$, it is observed that the base material exhibits a slightly higher FCGR value,

3.06×10^{-4} mm/cycle, compared to the uncoated and coated specimens tested in an aggressive medium, 3.04×10^{-4} mm/cycle and 2.95×10^{-4} mm/cycle. When the value of $\Delta K = 20$ MPa $\sqrt{m}$ is reached, the base material exhibits a crack growth rate of approximately 7.98×10^{-4} mm/cycle, in comparison to the base material tested in an aggressive medium, which shows a rate of 5.52×10^{-4} mm/cycle, and the coated material, which has a rate of 5.80×10^{-4} mm/cycle. This observation suggests that the inherent material properties of the base alloy may render it more susceptible to FCG under heightened stress intensity conditions, despite the external corrosive environment.

Research conducted in [9] on the 2524-T3 and 2198-T851 aluminium alloys in a seawater fog environment revealed that, for the same value of ΔK, the 2198-T851 aluminium alloy exhibits higher FCGRs when compared to the 2524-T3 alloy. In addition, as mentioned by the authors, this phenomenon is directly attributed to the presence of IM particles, which, due to their distinct properties, may act as either cathodic or anodic with respect to the aluminium matrix. As reported in [7], the corrosion mechanism of Al-Cu-Li alloys exposed to sodium chloride solution are complex and influenced by both micrometric and nanometric IM particles. Indeed, the context of third-generation aluminium alloys, such as 2198-T8, the main precipitates include δ (Al_3Li), T_1 (Al_2CuLi), θ' (Al_2Cu), and S (Al_2CuMg). Among these particles, the T_1 phase is particularly notable for its contribution to enhancing the mechanical strength of Al-Cu-Li alloys, as it forms on the {111} aluminium planes [34]. In reference [9], the authors mentioned that when Al-Cu-Li alloy is exposed to a solution containing chloride ions, such as that used in this study, the T_1 particles exhibit anodic behaviour when compared to the aluminium matrix, resulting in their dissolution. However, over time, as the lithium (Li) element preferentially corrodes, the copper (Cu) concentration on the surface of the aluminium matrix increases. The increased copper concentration shifts the electrochemical potential of the T1 particles to more positive values, rendering them cathodic relative to the aluminium matrix and driving a galvanic coupling effect that accelerates the localised corrosion process [35, 36]. On the SM, Figure SM2 presents schematic representations of the corrosion mechanism involved: Figure SM2(a) presents a schematic illustration of the galvanic coupling process related to the micrometric IM particles and the aluminium matrix, whilst Figure SM2(b) shows the corrosion mechanism associated with the nanometric IM intermetallic T_1.

In this context, when the 2198-T8 aluminium alloy is exposed to an aggressive chloride environment (0.6 mol L^{-1} NaCl solution), galvanic coupling processes occur, which are linked to the presence of both micro and nanometric IMs within the aluminium matrix. The pits that arise from this process act as stress concentrators and therefore affect the FCG curves, as can be seen by a comparison of Fig. 7(a) and (b). The presence of chloride ions accelerates the nucleation and formation of regions with a high density of pits, which exacerbates the fatigue process by creating localised areas of elevated stress concentration. Conversely, regarding the 2198-T8 aluminium alloy containing Nb_2O_5 thin films, it is evident that the FCGs are consistently lower than those of the uncoated material for $\Delta K < 14$ MPa $\sqrt{m}$.

Based on these results, it can be inferred that two mechanisms influence the FCG results: **(i)** For $\Delta K < 14$ MPa $\sqrt{m}$, the Nb_2O_5 thin film functions as a protective barrier, reducing the density of pits formed on the 2198-T8 aluminium alloy surface and thereby decreasing the crack growth rate values in 0.6 mol L^{-1} NaCl solution. On the other hand, as already demonstrated by this research group [20, 21], the coating produced by reactive sputtering technique on the surface of the 2198-T3 and 7050-T7451 aluminium alloys is not devoid of defects, which can facilitate the initiation of localised corrosion processes beneath the coating. Probably, the coating has a protective action in this range of ΔK. (ii) For $14 < \Delta K < 20$ MPa $\sqrt{m}$, the coated and uncoated 2198-T8 aluminium alloy exhibit a very similar behaviour in 0.6 mol L^{-1} NaCl solution, with FCGRs lower than the observed for the uncoated material in Laboratory air, and which can be explained, initially, by the action of corrosion products that are deposited at the crack interface, causing a wedge effect that favours crack closure. As reported by the literature [37], during the crack growth process, which entails loading and unloading cycles, the crack surfaces meet one another. Elber [38, 39] proposed that the growth of fatigue cracks is not governed by the nominal stress intensity factor range, DK, but by the effective stress intensity factor range instead, ΔK_{eff}. The ΔK_{eff} may be expressed by Eq. 5, and K_{op} denotes the crack opening stress intensity factor. A relationship between ΔK_{eff} and ΔK is established to quantify the effects of crack closure and can be expressed by Eq. 6. Here, U represents the quantitative parameter for the effects of crack closure and opening, respectively. The validation of the relationship proposed by Elber [38, 39] applies to the stress ratio range of $-0.1 < R < 0.7$, with ΔK varying between 13 and 40 MPa $\sqrt{m}$, and was demonstrated by using 2024-T3 aluminium alloy. In this sense, the fatigue crack growth (da/dN) may be written as a function of ΔK_{eff} and U, as displayed in Eq. 7.

$$\Delta K_{eff} = K_{max} - K_{op} \tag{5}$$

$$U = \frac{\Delta k_{eff}}{\Delta k} = \frac{k_{max} - k_{op}}{k_{max} - k_{min}} \tag{6}$$

$$\frac{da}{dN} = f(\Delta K_{eff}) = f(\Delta K, U) \tag{7}$$

As a supplementary material, Figure SM3 present optical images of the crack profiles, facilitating a comparative analysis of crack growth in both air and sodium chloride solution. Figures

SM3(a-c) depict the crack path of the 2198-T8 aluminium alloy exposed to air, highlighting three characteristic regions: lower ΔK, intermediate ΔK, and higher ΔK values. In contrast, Figures SM3(d-f) illustrate the 2198-T8 alloy subjected to a 0.6 mol L^{-1} NaCl solution. Finally, Figure SM3(g-i) present the crack path of the coated 2198-T8 alloy also exposed to the 0.6 mol L^{-1} NaCl solution. The morphological results compellingly demonstrate that the 2198-T8 aluminium alloy, when exposed to an aggressive environment, exhibits a highly corroded surface in comparison to the coated material. The analysis reveals an extensive amount of corrosion products, accompanied by the formation of pits, which indicate an accelerated corrosion process. This remarkable difference in surface integrity underscores the deleterious impact of adverse environmental conditions on the uncoated alloy, highlighting the effectiveness of the Nb_2O_5 coating in protecting against corrosion and mitigating corrosion processes. Figure 8 presents a schematic representation of the fracture surface features of the 2198-T8 aluminium alloy, as analysed using scanning electron microscopy (SEM) after air exposure. In Fig. 8(a), micrographs of the notch region are displayed, while Fig. 8(b-d) and (e–g) illustrate the intermediate and high values of ΔK, respectively. In Fig. 8(d), larger striation bands, typically associated with ductile fracture mechanisms, are observable. Conversely, the zoomed-in regions presented in Fig. 8(e–g) reveal smaller striation bands. Additionally, backscattered electron (BSE) micrographs of these smaller striation bands are illustrated in Fig. 8(h, i). The average measured width of these marks is approximately 0.41 μm, which within a margin of error, is in accordance with the literature [40–42].

The protective effect of the Nb_2O_5 thin film is further corroborated by SEM images of the fracture surface presented by comparison of Fig. 9. As illustrated in Fig. 9(a), which pertains to the fracture surface of Region II (characterised by intermediate ΔK values), the 2198-T8 aluminium alloy when exposed to a 0.6 mol L^{-1} NaCl solution shows the presence of pits. As reported by the literature [30, 43, 44], pitting is a highly localised form of corrosion induced by aggressive chloride ions and represents the predominant mode of corrosive attack observed in aluminium alloys. In addition, the presence of inclusions, IM particles, second-phase particles, and mechanical damage can serve as preferential sites for pitting nucleation. The corresponding EDX maps for the elements aluminium (Al), oxygen (O), and copper (Cu) can be found in Fig. 9(b-d), respectively. Figure 9(e) presents the micrograph of the 2198-T8/Nb_2O_5 following fracture. Generally, it can be observed that an anhydrous oxide film has formed, along with areas exhibiting characteristics of mudcracking, which is commonly observed in aluminium alloys. In this case, the extensive presence of corrosion products hindered the identification of regions containing pits. Figure 9(f–j) display the EDX maps for the sample 2198-T8/Nb_2O_5, showcasing the presence of Al, O, Cu, Nb and Cl, respectively.

Figure 10(a–f) show the EBSD inverse pole figure (IPF) maps for the 2198-T8 aluminium alloy under different testing conditions. The IPF maps provide insights into the crystallographic orientations along the crack path, revealing distinct differences in deformation and grain boundary characteristics between the tested conditions. In air, as shown in Fig. 10(a) and (d), the crack path predominantly follows transgranular propagation with minimal evidence of localised deformation, consistent with a relatively uniform stress distribution and ductile fracture mechanisms. In contrast, the IPF maps in Fig. 10(b) and (e) illustrate the crack path for the alloy exposed to a 0.6 mol L^{-1} NaCl solution, where a notable increase in grain boundary interaction is observed, suggesting an influence of environmental corrosion on the crack propagation mechanism. The maps reveal a combination of transgranular and intergranular propagation, driven by localised corrosion at grain boundaries, resulting in a more tortuous crack path indicative of the synergistic effects of mechanical stress and corrosive attack. Figure 10(c) and (f) present the IPF maps for the 2198-T8/Nb_2O_5-coated alloy exposed to the same NaCl solution, showing a reduced degree of grain boundary interaction and a more uniform transgranular propagation compared to the uncoated alloy. This behaviour highlights the protective efficacy of the Nb_2O_5 coating in mitigating corrosion-assisted cracking by effectively limiting the ingress of the corrosive solution, thereby reducing localised stress concentration and preserving the integrity of the grain boundaries. This remarkable difference in surface integrity underscores the deleterious impact of adverse environmental conditions on the uncoated alloy, highlighting the effectiveness of the Nb_2O_5 coating in protecting against corrosion and mitigating corrosion processes.

Conclusions

In conclusion, this study provided compelling evidence of the significant enhancement in corrosion as well as corrosion-fatigue resistance afforded to 2198-T8 aluminium alloy through the utilisation of reactive sputtering technique to produce Nb_2O_5 coatings. The observed reduction in fatigue crack growth rates is substantial under aggressive chloride environments, and, coupled with the improved electrochemical stability demonstrated by uniform corrosion tests, confirm therefore the protective efficacy of the Nb_2O_5 coatings. The mechanism of corrosion protection appears multifaceted, involving both the provision of a physical barrier against corrosive ingress and the modification of the alloy's surface electrochemical behaviour. While the coating itself exhibited minor imperfections, its overall impact on mitigating both, uniform and localised corrosion, alongside fatigue-induced crack growth, is demonstrably positive. These findings offer valuable insights for the development of advanced protective strategies for aluminium alloys intended for

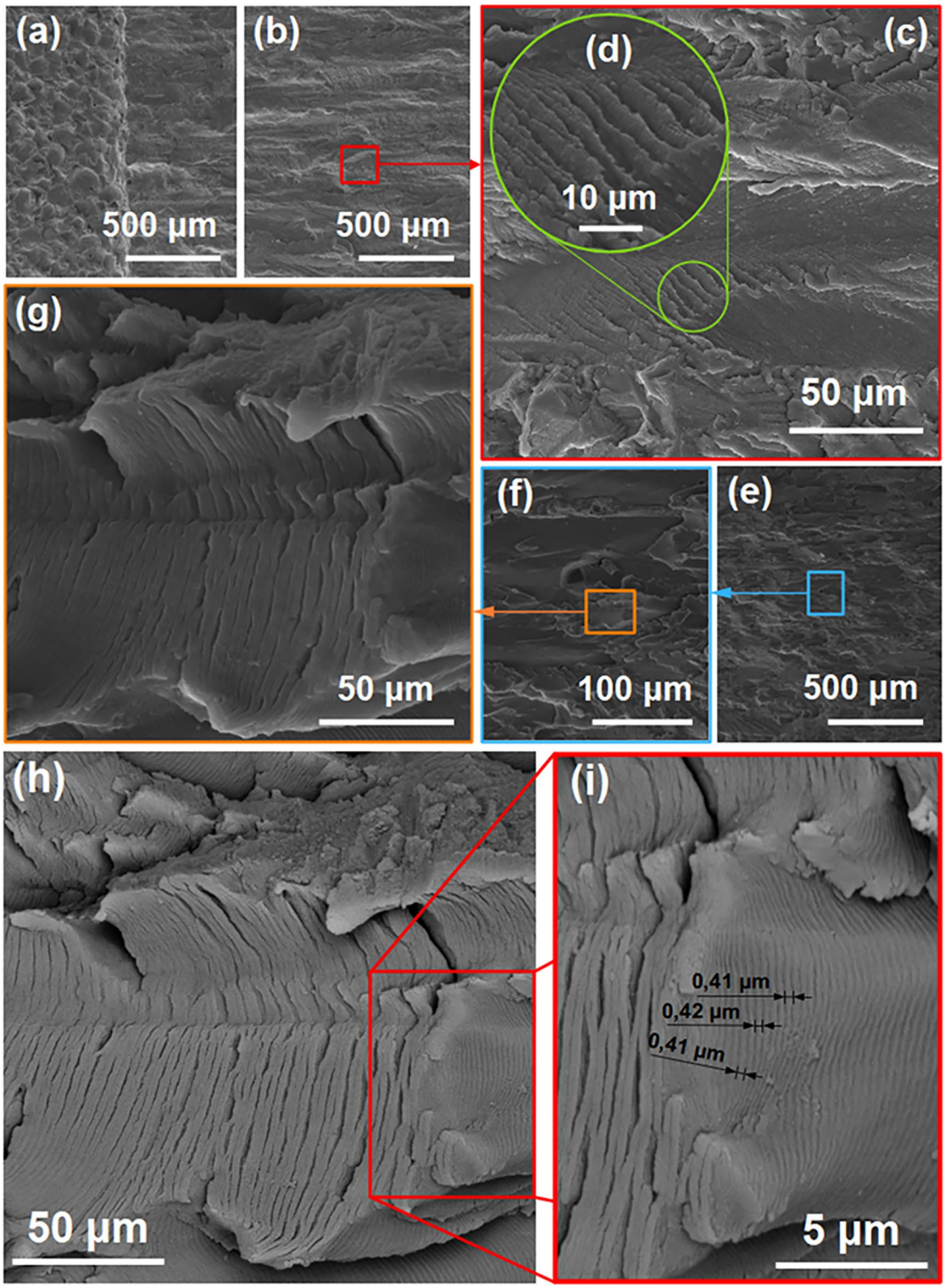

Figure 8: Micrographs of the fracture surfaces. (a) notch region; (b–d) intermediate values of ΔK; (e–g) high values of ΔK; (h, i) BSE images showing the spacing between the slip bands. These micrographs are of the 2198-T8 alloy tested in air.

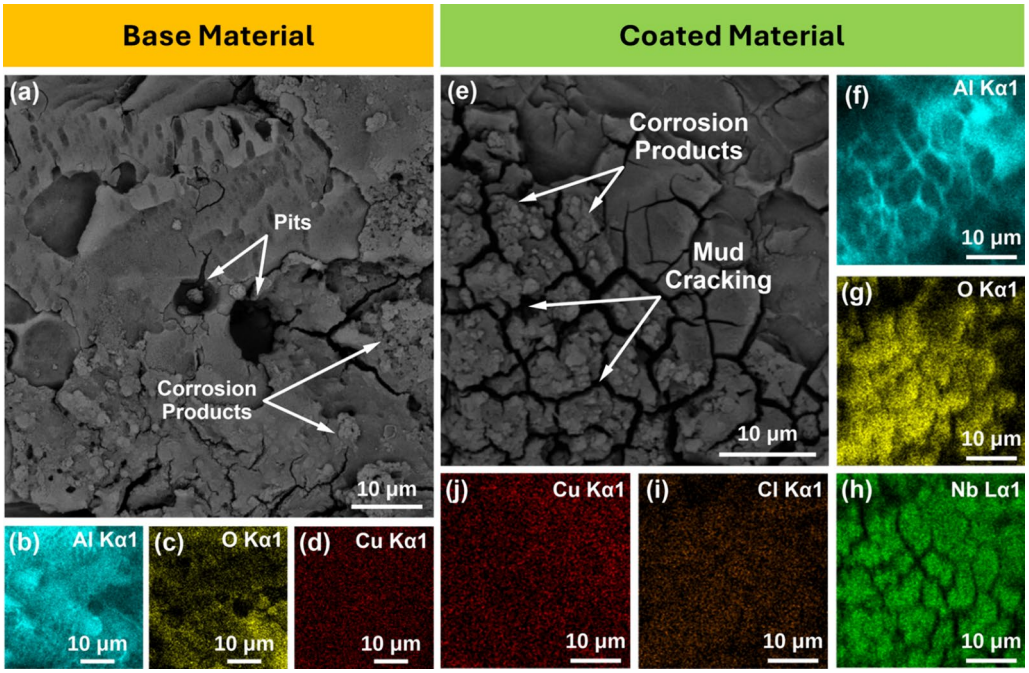

Figure 9: Micrographs and EDX spectrum of the fracture surface. (a) uncoated 2198-T8 aluminium alloy exposed to 0.6 mol L^{-1} NaCl solution, (b–d) respective EDX maps; (e) coated 2198-T8 aluminium alloy surface exposed to 0.6 mol L^{-1} NaCl solution; (f–j) respective EDX maps.

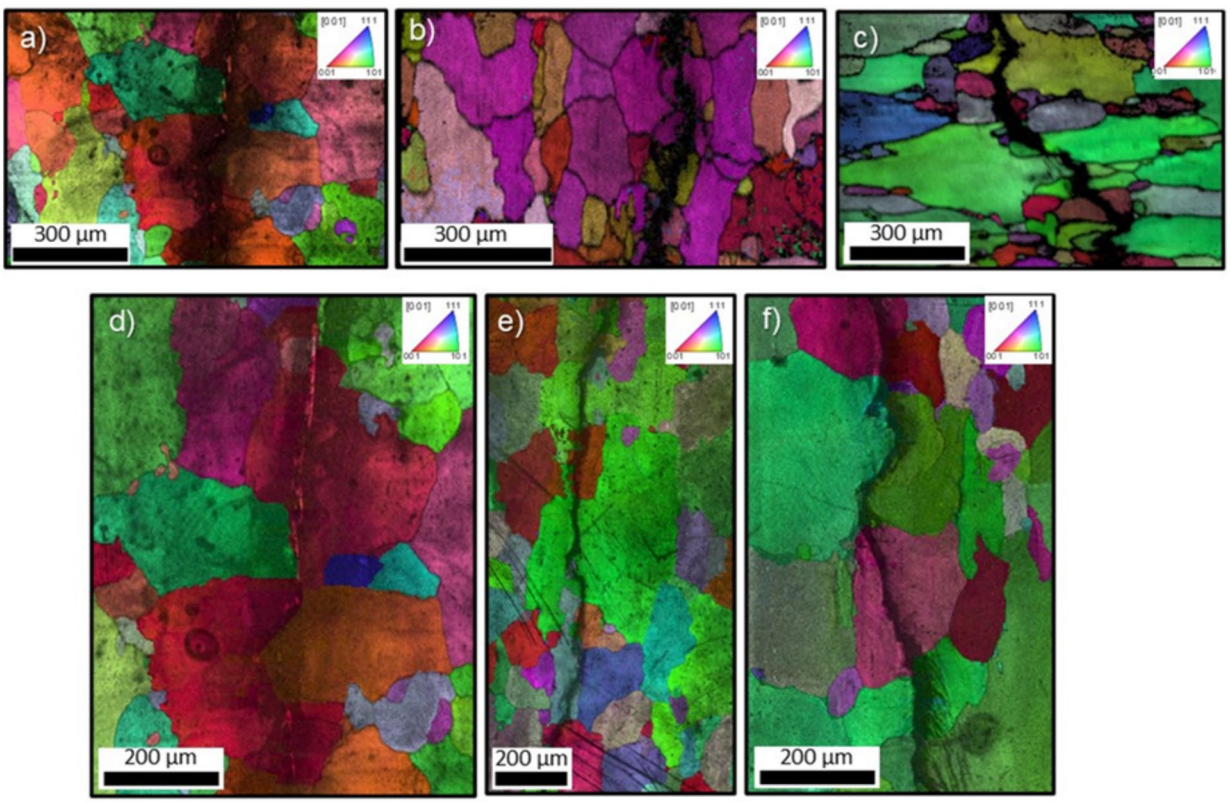

Figure 10: Inverse Pole Figure (IPF) maps illustrating the crack path in 2198-T8 aluminium alloy under different testing conditions. (a) notch-to-mid crack region and (d) mid-to-final crack region tested in air; (b) notch-to-mid crack region and (e) mid-to-final crack region exposed to a 0.6 mol L^{-1} NaCl solution; (c) notch-to-mid crack region and (f) mid-to-final crack region for 2198-T8/Nb_2O_5 aluminium alloy exposed to a 0.6 mol L^{-1} NaCl solution.

high-performance applications, particularly within the demanding operational conditions encountered in the aerospace sector.

Experimental

Material

The 2198-T8 aluminium alloy was used in this study as-received condition, with its chemical composition (wt%) being referenced from [45]. As previously stated, the objective of this research was to investigate the impact of Nb_2O_5 coatings on the corrosion as well as the corrosion-fatigue resistance of this material. In this context, the mentioned studies were conducted on both the base material samples and those coated with Nb_2O_5 thin films.

Samples preparation

Prior to the deposition process, the samples, approximately 2 mm thick, were subjected to grinding using silicon carbide (SiC) abrasive papers in a sequential range of 800, 1200, 2400, and 4000 *mesh*. Following this, the samples were polished with chromium oxide (Cr_2O_3) and diamond pastes of varying particle sizes (3, 1, and 0.25 μm). Subsequently, the samples were rinsed with distilled water and isopropyl alcohol for a duration of 10 min before being stored in suitable locations.

Deposition process

Nb_2O_5-based coatings were deposited on the surfaces of the 2198-T8 aluminium alloy by using the reactive sputtering technique installed at Thin Film and Plasma Process Laboratory, Institute of Technological and Exact Sciences (ICTE), University of Triângulo Mineiro (UFTM), Minas Gerais, Brazil. The deposition system consists of a magnetron sputtering apparatus sourced from Kurt Lesker Co. designed for 2.0-inch diameter targets. Vacuum support is maintained by a combination of rotary and turbomolecular pumps, ensuring a base pressure of 0.001 mTorr. Film depositions were performed at a pressure of 5.0 mTorr, utilizing Argon (99.999% purity, White Martins) in conjunction with a Niobium target (99.9% purity) provided by CBMM-Brazil. To achieve the formation of Nb_2O_5 coatings, O_2 (99.999% purity, White Martins) was introduced at a pressure of 0.5 mTorr. The applied DC voltage and current during the process were 450 V and 145 mA, respectively. It is very important to emphasise that the Nb_2O_5 coatings were deposited at 300 °C. Figure SM4 on the supplementary material presents a schematic representation of the device employed for the deposition of Nb_2O_5 thin films on the surface of the 2198-T8 alloy. Additional information regarding the produced thin films can be found in the references provided [20–25].

Morphological and structural characterisations

The optical microscopy analyses were conducted by using the ZEISS Optical Microscope Axio Scope.A1 in the Materials Engineering Department (SMM) at the School of Engineering of São Carlos (EESC) at the University of São Paulo (USP), São Carlos, Brazil. The morphology and thickness profiles of the Nb_2O_5 coating were also evaluated using Atomic Force Microscopy (AFM) with a Shimadzu SPM9700 microscope, employing dynamic mode and cantilevers procured from NT-MDT Co. AFM measurements were performed at the Institute of Technological and Exact Sciences (ICTE), University of Triângulo Mineiro (UFTM), Minas Gerais, Brazil.

The morphology of the 2198-T8 aluminium alloy specimens, both before and after undergoing corrosion and fatigue-corrosion tests, was evaluated using SEM/EDX. For this analysis, a field emission gun scanning electron microscope (FEG-SEM) model JEOL 7001, equipped with an Oxford light elements EDX detector, was employed. These analyses were conducted in the Chemistry Department at the University of Uberlândia (UFU), Minas Gerais, Brazil.

The FTIR spectrum was obtained by using an Agilent Care 600 equipment and specular reflection accessory purchase from Pike Co. installed at the Institute of Technological and Exact Sciences (ICTE), Federal University of Triângulo Mineiro (UFTM), Minas Gerais, Brazil. The wavenumber range from 4000 to 400 cm^{-1} was used, collecting 64 scans with resolution of 4 cm^{-1}.

Raman measurements were performed in a Renishaw inVia™ Qontor TM confocal Raman microscope equipped with a Peltier cooled to -70 °C for ultra-low noise charge-coupled device (CCD) Centrus 2957T3 detector and an Nd:YAG laser operating at 32 mW of 532 nm laser excitation, and a diffraction grating with 1800 l/mm. The spectral resolution of the spectroscopic system is 0.3 cm^{-1}. The laser beam was focused with a 100 × Leica objective lens (N Plan EPI) with a numerical aperture of 0.85. To map the sample surface, an area of 49.0 × 46.0 m was scanned with a 1.0 m step, resulting in 2254 collected spectra. An integration time of 2 scans of 0.4 s each was used for all measurements to reduce the random background noise induced by the detector, without significantly increasing the acquisition time. The incident laser intensity was 3.2 mW (10% of the maximum laser power). Between different Raman sessions, the spectrograph was calibrated using the Raman line at 520.5 cm^{-1} of an internal Si wafer to reduce possible fluctuations of the Raman system. To avoid the contribution of the substrate in the measurements, self-supported multilayer graphene substrates were used for this study, resulting in spectra with well-defined bands.

The EBSD analysis was used in the present survey for crystallographic observations near the main crack for the

uncoated and coated 2198-T8 aluminium alloy. It is important to emphasize that this procedure was adopted for the 2198-T8 aluminium alloy specimens removed on the LT direction. EBSD analyses were conducted using a 4th-generation MIRA scanning electron microscope from TESCAN to characterise aluminium samples at the Department of Material Engineering of the Federal University of São Carlos, UFSCar, São Carlos, São Paulo, Brazil. To ensure stability during preparation and analysis, the samples were embedded in resin and subsequently subjected to progressive grinding with abrasive papers of increasing grit sizes (120, 220, 320, 400, 600, 1200, and 1500) to achieve a smooth and flat surface. Following grinding, the samples were polished using a Vibratory Polisher (Buehler) with colloidal silica as the abrasive agent to remove residual marks and microimperfections, creating an optimal surface for EBSD analysis. To further enhance the EBSD signal quality, an additional electrolytic polishing step was performed using Polimat 2 (Buehler) equipment with an electrolyte solution of perchloric acid (20% v/v) and ethyl alcohol (80% v/v). This final polishing step ensured a superior surface finish, maximising the resolution and accuracy of the EBSD data.

Corrosion studies

Global corrosion tests were conducted to investigate the influence of the Nb_2O_5 coating on the electrochemical behaviour of the 2198-T8 aluminium alloy. The OCP was monitored over a period of 3 h to assess the thermodynamic stability of the material both with and without Nb_2O_5 coatings in 0.6 mol L^{-1} NaCl solution. Additionally, the OCP measurements facilitated the determination of the potential window that was used in the PP tests. The PP tests enabled the characterization of the anodic and cathodic domains, as well as the determination of the i_{corr}, E_{corr}, and $E_{pitting}$. EIS measurements were obtained over a frequency range of 100 kHz to 10 mHz, employing a sinusoidal perturbation of 10 mV (rms) and various immersion times, specifically: 3, 6, 12, 24, 72 and 168 h of immersion in 0.6 mol L^{-1} NaCl solution. Typically, EIS spectra were obtained at the E_{OCP}. However, as demonstrated by Moreto et al. [4, 9], when 2xxx series aluminium alloys are exposed to sodium chloride solution, $E_{pitting}$ and E_{corr} are often nearly the same. Consequently, even a slight increase in potential above E_{corr} can induce or accelerate pitting, leading to a significant increase in anodic current density. This results in non-linearity and compromises the validity of the EIS measurements. For this reason, in the present work the EIS tests were conducted at -20 mV *versus* E_{corr} [4]. All the electrochemical tests were conducted using a conventional three-electrode electrochemical cell, which included a working electrode (2198-T8 and 2198-T8/Nb_2O_5), a platinum counter electrode (Pt), and a saturated calomel reference electrode (Hg/Hg_2Cl_2, KCl_{sat}) at room temperature. A μStat-i 400 potentiostat/galvanostat was employed at Materials Engineering Department (SMM) at São Carlos School of Engineering (EESC), University of São Paulo (USP), São Paulo, Brazil. The electrochemical tests were complemented by an extensive characterization utilising optical microscopy and SEM/EDX both before and after the tests.

Corrosion-fatigue tests

As mentioned by the ASTM-E647 [46], the FCG expressed as a function of crack-tip stress-intensity factor range, da/dN versus ΔK, characterizes a material's resistance to stable crack extension under cyclic loading. Here, FCG tests were conducted on middle-tension specimens (M(T)) with and without Nb_2O_5 coatings on the crack growth region. For this purpose, a 100 kN closed-loop servo-hydraulic testing machine was employed to obtain the FCG curves. Prior to the FCG tests, a precise precracking of 1 mm was introduced at the centre of both coated and uncoated M(T) specimens. The introduction of the precracking is crucial as it ensures a sharpened fatigue crack of adequate size, straightness, and symmetry in the M(T) specimen. The FCG tests were conducted under controlled loading conditions, using a sinusoidal waveform at frequencies of 10 Hz (in air) and 1 Hz (in 0.6 mol L^{-1} NaCl solution), with a load ratio (R) of 0.1. Crack length monitoring was performed using the compliance method with an MTS 632.30 C-20 clip gauge. An experimental setup constructed to perform corrosion-fatigue tests may be seen in Figure SM5 of the supplementary material. The illustration provides detailed information regarding the 100 kN closed-loop servo-hydraulic machine, the solution storage system, the acrylic cell, and their respective inputs and outputs for the circulation of the 0.6 mol L^{-1} NaCl solution, as well as the dimensions of the M(T) specimens in accordance with ASTM E-647 [46]. Corrosion-fatigue tests were performed at the SMM-EESC-USP, São Carlos, Brazil.

Acknowledgments

J. A. Moreto would like to acknowledge the financial support received from the National Council for Scientific and Technological Development (CNPq-Brazil) (Grants 303659/2019-0, 402988/2021-3, 302770/2022-4) and the São Paulo Research Foundation (FAPESP 2024/02504-0). R.V. Gelamo would like to thank the National Council for Scientific and Technological Development (CNPq-Brazil) (Grant 302582/2021–5), Fapemig (Grant APQ-05247-23), the Brazilian Institute of Science and Technology (INCT) in Carbon Nanomaterials, and CBMM. This work received funding from the FCT (Fundação para a Ciência e Tecnologia, I.P.) under the project's LA/P/0037/2020, UIDP/50025/2020, and UIDB/50025/2020 of the Associate Laboratory Institute of Nanostructures, Nano modelling and Nanofabrication—i3N. The authors Uriel Darhê Oudinot Dias Rangel and Murilo Oliveira Alves Ferreira thank the Coordination for

the Improvement of Higher Education Personnel (CAPES-Brazil) for the master's scholarship. J. A. Moreto, R. V. Gelamo, C. A. R. Baptista, G. Y. Koga and H. C. Pinto are CNPq fellows.

Author contributions

Uriel Darhê Oudinot Dias Rangel: Investigation, Formal analysis and writing-up, Murilo Oliveira Alves Ferreira: Investigation and Formal analysis, Natália Bueno Leite Slade: Formal analysis, Rogério Valentim Gelamo: Investigation, Carlos Antônio Reis Pereira Baptista: Formal analysis, Haroldo Cavalcanti Pinto: Formal analysis, Igor Mota: Investigation, Guilherme Yuki Koga: Investigation and Formal analysis, Hugo Manuel Brito Águas: Formal analysis, Witor Wolf: Investigation and Formal analysis, Jéferson Aparecido Moreto: Investigation, Formal analysis, writing-up, and project administration.

Funding

Conselho Nacional de Desenvolvimento Científico e Tecnológico, 303659/2019-0, Jéferson Aparecido Moreto, 402988/2021-3, Jéferson Aparecido Moreto, 302770/2022-4, Jéferson Aparecido Moreto, 302582/2021–5, Rogério Valentim Gelamo, Fundação de Amparo à Pesquisa do Estado de São Paulo, FAPESP 2024/02504-0, Jéferson Aparecido Moreto, Fundação para a Ciência e a Tecnologia (FCT), LA/P/0037/2020, Hugo Manuel Brito Águas, UIDP/50025/2020, Hugo Manuel Brito Águas, UIDB/50025/2020, Hugo Manuel Brito Águas, Coordenação de Aperfeiçoamento de Pessoal de Nível Superior, Uriel Darhê Oudinot Dias Rangel and Murilo Oliveira Alves Ferreira.

Data availability

Not applicable.

Code availability

Not applicable.

Declarations

Conflict of interest The authors declare that they have no known competing financial interests or personal relationships that could have appeared to influence the work reported in this paper.

Supplementary Information

The online version contains supplementary material available at https://doi.org/10.1557/s43578-025-01631-6.

Open Access

References

1. P. Dwivedi, A.N. Siddiquee, S. Maheshwari, Russ. J. Non-Ferr. Metals (2021). https://doi.org/10.3103/S1067821221020048
2. R.J. Raj, P.P. Selvam, M. Pughalendi, J. Huazhong Univ. Sci. Technol. **1671**, 4512 (2021)
3. P. Rambabu, N. Eswara Prasad, V.V. Kutumbarao, R.J.H. Wanhill, Aluminium Alloys for Aerospace Applications, in *Aerospace Materials and Material Technologies – Volume 1: Aerospace Materials*. ed. by N. Eswara Prasad, R.J.H. Wanhill (Springer, Singapore, 2017)
4. J.A. Moreto, C.E.B. Marino, W.W. Bose Filho, L.A. Rocha, J.C.S. Fernandes, Corros. Sci. (2014). https://doi.org/10.1016/j.corsci.2014.03.001
5. U. Donatus et al., BoD–Books on Demand, in *Advanced Aluminium Composites and Alloys*. ed. by L.A. Dobrzański (IntechOpen, London, 2021)
6. J.V. de Sousa Araujo, R.M.P. da Silva, B.V. Viveiros, M.X. Milagre, C. de Souza Carvalho Machado, I. Costa, Quim. Nova. (2022). https://doi.org/10.21577/0100-4042.20170874
7. M.O.A. Ferreira, J.P.L. Nascimento, N.B. Leite, A. de Siervo, G.L. Fernandes, A.R. Vaz, R.V. Gelamo, I.V. Aoki, J.A. Moreto, Mater. Res. (2023). https://doi.org/10.1590/1980-5373-MR-2022-0453
8. J.F. Li, C.X. Li, Z.W. Peng, W.J. Chen, Z.Q. Zheng, J. Alloys Compd. (2008). https://doi.org/10.1016/j.jallcom.2007.06.072
9. J.A. Moreto, E.E. Broday, L.S. Rossino, J.C.S. Fernandes, W.W. Bose Filho, J. Mater. Eng. Perform. (2018). https://doi.org/10.1007/s11665-018-3244-7
10. V. Aryshenskii, F. Grechnikov, E. Aryshenskii, Y. Erisov, S. Konovalov, M. Tepterev, A. Kuzin, Materials (2022). https://doi.org/10.3390/ma15207062
11. Y. Zhu, K. Sun, G.S. Frankel, J. Electrochem. Soc. (2018). https://doi.org/10.1149/2.0931811jes
12. R. Wu, Z. Liu, H. Ning, D. Lu, Z. Liu, Y. Meng, J. Li, R. Zhang, Metals (2023). https://doi.org/10.3390/met13020341
13. G.T. Burstein, C. Liu, R.M. Souto, S.P. Vines, Corros. Eng. Sci. Technol. (2004). https://doi.org/10.1179/147842204225016859

14. G.S. Frankelt, J. Electrochem. Soc. (1998). https://doi.org/10.1149/1.1838615
15. F. Mansfeld, S. Lin, S. Kim, H. Shih, J. Electrochem. Soc. (1990). https://doi.org/10.1149/1.2086442
16. L.M.P. de Lacerda, R.V. Gelamo, L.S. de Almeida, L.S. Rossino, C.E.B. Marino, J.C.S. Fernandes, J.A. Moreto, : Electron. J. Chem. (2019). https://doi.org/10.17807/orbital.v11i2.1321
17. M.O.A. Ferreira, K.R. dos Santos, D.G. Bon, R.V. Gelamo, R. Galo, N.B. Leite, C.A.R.P. Baptista, H.C. Pinto, J.A. Moreto, Emergent. Mater. (2024). https://doi.org/10.1007/s42247-024-00746-6
18. L.R. Freitas, R.V. Gelamo, C.E.B. Marino, J.P.L. Nascimento, J.M.A. Figueiredo, J.C.S. Fernandes, J.A. Moreto, Surf. Coat. Technol. (2022). https://doi.org/10.1016/j.surfcoat.2022.128197
19. U.D.O.D. Rangel, R. Borges, D.A. Oliveira, L.S. de Almeida, R.V. Gelamo, J.R.S. Júnior, L.S. Rossino, J.A. Moreto, Mater. Res. (2019). https://doi.org/10.1590/1980-5373-MR-2018-0593
20. J.A. Moreto, R.V. Gelamo, J.P.L. Nascimento, M. Taryba, J.C.S. Fernandes, Appl. Surf. Sci. (2021). https://doi.org/10.1016/j.apsusc.2021.149750
21. M.O.A. Ferreira, G.T.L. Teixeira, N.B. Leite, R.V. Gelamo, H.C. Pinto, I.V. Aoki, J.A. Moreto, Emerg. Mater (2023). https://doi.org/10.1007/s42247-023-00569-x
22. J.P.L. Nascimento, G.T.L. Teixeira, M.M.S. Obata, M.V. Silva, C.J.F. Oliveira, L.E.A. Silva, R.V. Gelamo, N.B.L. Slade, J.A. Moreto, Mater. Res. (2023). https://doi.org/10.1590/1980-5373-MR-2023-0251
23. M.C. de Almeida Bino, W.A. Eurídice, R.V. Gelamo, N.B. Leite, M.V. da Silva, A. de Siervo, M.R. Pinto, P.A. de Almeida Buranello, J.A. Moreto, Appl. Surf. Sci. (2021). https://doi.org/10.1016/j.apsusc.2021.149739
24. J.P.L. do Nascimento, M.O.A. Ferreira, R.V. Gelamo, J. Scarmínio, T.T. Steffen, B.P. da Silva, I.V. Aoki, A.G. dos Santos, V.V. de Castro, C. de Fraga Malfatti, J.A. Moreto, Surf. Coat Technol. (2021). https://doi.org/10.1016/j.surfcoat.2021.127854
25. J.A. Moreto, R.V. Gelamo, M.V. da Silva, T.T. Steffen, C.J.F. de Oliveira, P.A. de Almeida Buranello, M.R. Pinto, J. Mater. Sci. Mater. Med. (2021). https://doi.org/10.1007/s10856-021-06498-7
26. A.A. McConnell, J.S. Aderson, C.N.R. Rao, Spectrochim. Acta A (1976). https://doi.org/10.1016/0584-8539(76)80291-7
27. J.M. Jehng, I.E. Wachs, Chem. Mater. (1991). https://doi.org/10.1021/cm00013a025
28. B. Orel, M. Maček, J. Grdadolnik, A. Meden, J. Solid State Electrochem. (1998). https://doi.org/10.1007/s100080050092
29. K. Nakamoto, *Infrared and Raman Spectra of Inorganic and Coordination Compounds*, 6th edn. (Wiley, Hoboken, 2008). https://doi.org/10.1002/9780470405840
30. N. Kemal, in *Corrosion Behaviour and Protection of Copper and Aluminium Alloys in Seawater*. ed. by D. Féron (Woodhead Publishing Limited, Cambridge, 2007), p.145
31. J.A. Moreto, M.S. dos Santos, M.O.A. Ferreira, G.S. Carvalho, R.V. Gelamo, I.V. Aoki, M. Taryba, W.W. Bose Filho, J.C.S. Fernandes, Corros. Sci. (2021). https://doi.org/10.1016/j.corsci.2021.109253
32. R.P. Wei, G.W. Simmons, Int. J. Fract. (1981). https://doi.org/10.1007/BF00053522
33. A.M.L. Adib, C.A.R.P. Baptista, Mater. Sci. Eng. A (2007). https://doi.org/10.1016/j.msea.2006.10.124
34. R.J. Rioja, J. Liu, Metall. Mater. Trans. A (2012). https://doi.org/10.1007/s11661-012-1155-z
35. J.V.S. de Araujo, R.M.P. da Silva, B.V.G. de Viveiros, R.E. Klumpp, I. Costa, Matéria (Rio J) (2024). https://doi.org/10.1590/1517-7076-RMAT-2023-0328
36. J.V. De Sousa Araujo, R.M.P. Da Silva, U. Donatus, C. De Souza Carvalho, I.C. MacHado, Mater. Res. (2020). https://doi.org/10.1590/1980-5373-MR-2020-0161
37. V. Ribeiro, J. Correia, G. Lesiuk, A. Gonçalves, A. De Jesus, F. Berto, Int. J. Fatigue (2021). https://doi.org/10.1016/j.ijfatigue.2021.106472
38. W. Elber, in *Damage Tolerance in Aircraft Structures*. ed. by M. Rosenfeld (ASTM International, West Conshohocken, 1971), p.230
39. W. Elber, Fatigue crack closure under cyclic tension. Eng. Fract. Mech. (1970). https://doi.org/10.1016/0013-7944(70)90028-7
40. A. Cini, P. Irving, Fatigue. Fract. Eng. Mater. Struct. (2017). https://doi.org/10.1111/ffe.12544
41. Y. Uchida, M. Shimojo, Y. Higo, J. Mater. Sci. (1999). https://doi.org/10.1023/A:1004510615621
42. P. Martin, J.I. Dickson, J.-P. Baïlon, Mater. Sci. Eng. (1985). https://doi.org/10.1016/0025-5416(85)90402-1
43. C. Vargel, *in Corrosion of Aluminium* (Elsevier, Amsterdam, 2020)
44. N.J.H. Holroyd, G.M. Scamans, R.C. Newman, A.K. Vasudevan, Aluminum-Lithium Alloys, in *Aluminum-Lithium Alloys*. ed. by N. Eswara Prasad, A.A. Gokhale, R.J.H. Wanhill (Butterworth-Heinemann, New York, 2014)
45. J.V. de Sousa Araujo, M.X. Milagre, R.O. Ferreira, C. de Souza Carvalho Machado, C.P. de Abreu, I. Costa, Metallogr. Microstruct. Anal. (2020). https://doi.org/10.1007/s13632-020-00688-5
46. ASTM International (2013). https://doi.org/10.1520/E0647-13E01.